Wind turbine wake characterization using the SpinnerLidar measurements

Conti, Davide; Dimitrov, Nikolay Krasimirov; Peña, Alfredo; Herges, Thomas

Published in:
Journal of Physics: Conference Series

Link to article, DOI:
10.1088/1742-6596/1618/6/062040

Publication date:
2020

Document Version
Publisher's PDF, also known as Version of record

Wind turbine wake characterization using the SpinnerLidar measurements

Wind turbine wake characterization using the SpinnerLidar measurements

Davide Conti[1], Nikolay Dimitrov[1], Alfredo Peña[1] and Thomas Herges[2]

[1] Department of Wind Energy, Technical University of Denmark, Roskilde, Denmark
[2] Sandia National Laboratories, Albuquerque, New Mexico, USA

E-mail: davcon@dtu.dk

Abstract. We analyze SpinnerLidar measurements of a single wind turbine wake collected at the SWiFT facility and investigate the wake behaviour under different atmospheric turbulence conditions. The derived wake characteristics include the wake deficit, wake-added turbulence and wake meandering in both lateral and vertical directions. The atmospheric stability at the site is characterized using observations from a sonic anemometer. A wake-tracking technique, based on a bi-variate Gaussian wake shape, is implemented to monitor the wake center displacements in time to derive quasi-steady wake deficit and turbulence profiles in a meandering frame of reference. The analysis demonstrates the influence of atmospheric stability on the wake behaviour; a faster wake deficit recovery and a higher level of turbulence mixing are observed under unstable compared to stable atmospheric conditions. We also show that the wake meandering is driven by large-scale turbulence structures, which are characterized by increasing energy content as the atmosphere becomes more unstable. These results suggest the suitability of the dataset for wake-model calibration and provide statistics of the wake deficit, turbulence levels, and meandering, which are key aspects for load validation studies.

1. Introduction

Wind turbines are generally installed in large clusters and experience wake-induced effects during operation. The wake-affected flow fields are characterized by strong velocity deficits and increased turbulence levels, which lead to lower power productions and higher loading conditions compared to operation in free wind conditions [1]. To date, wake-induced effects on wind turbine operation are predicted using engineering-like wake models, due to their computationally efficiency. The IEC 61400-1 (2019) standard recommends the use of the Dynamic Wake Meandering model (DWM) [2], among few other approaches, for this purpose. The accuracy of DWM-based wake characteristics and resulting power and load predictions depends on the intrinsic simplifications of the model formulation, among others. However, due to the complexity of wake fields, the DWM and analytical wake models in general are prone to a significant level of uncertainty. The work of [3] quantified deviations between DWM-based and measured fatigue loads in the range of 11–15% for the tower bottom and 8–21% for the blade-root flapwise bending moment. In this regard, high-resolution measurements of the wake performed by nacelle-mounted lidars can potentially reduce the uncertainty in load predictions, through appropriate wake-model calibration. In the present work, we analyze data collected

at the SWiFT facility during a wake characterization and steering campaign that took place between 2016 and 2017 [4, 5]. The objective of this work is to derive wake characteristics from the SpinnerLidar measurements, and to study the influence of incoming wind conditions on wake features such as wake deficit, wake-added turbulence and wake meandering.

2. Measurement campaign

The measurement campaign was conducted at the SWiFT facility located in Lubbock, Texas, operated by Sandia National Laboratories. Figure 1 provides a schematic illustration of the experiment layout. The present work focuses on the dataset collected at the meteorological mast (METa1), the Vestas V27 wind turbine (WTGa1), and the DTU SpinnerLidar mounted on the nacelle of the WTGa1 and looking backwards. The WTGa1 is a variable-speed and pitch-regulated turbine with hub height of 32.1 m and rotor diameter D = 27 m. The METa1 (hereafter the mast) is instrumented with sonic anemometers mounted at 10, 18, 32, 45 and 58 m, sampling at 100 Hz, among other instruments. As southerly winds are prevalent at the site, this layout allows to retrieve simultaneous atmospheric inflow wind conditions at the mast, and wake measurements behind WTGa1 through the SpinnerLidar. The full site instrumentation is described in [4].

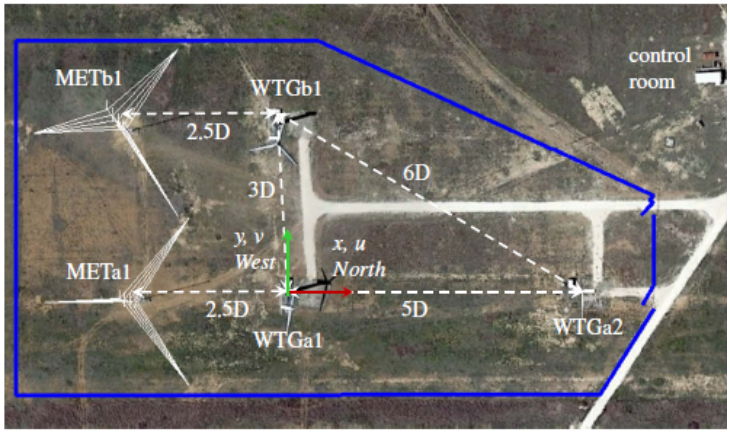

Figure 1. Top view of the SWiFT facility layout, source [4]. The geographical North is pointing toward the right side of the figure for illustrative purposes only. The wind turbines and met masts are shown and the spacing is normalized over the rotor diameters D.

2.1. Lidar scanning patterns

The SpinnerLidar is a continuous-wave wind lidar that scans in a two-dimensional plane [6]. For the SWiFT experiment, the SpinnerLidar scans the wake affected flow field behind the WTGa1, by sampling 984 line-of-sight velocity measurements (LOS) in a rosette-curve pattern (see Fig. 2). Two scanning strategies were adopted: scanning over multiple focused distances (between 1 D and 5 D), and scanning at a single focused distance (2.5 D). In the first strategy, the SpinnerLidar scans each distance every $\approx 32 - 42$ s, providing insights on the wake evolution at several downstream distances. The second strategy is tailored to scan at a single distance every ≈ 2 s, thus better allowing the estimation of second-order statistics of the velocity components and meandering dynamics [5, 7].

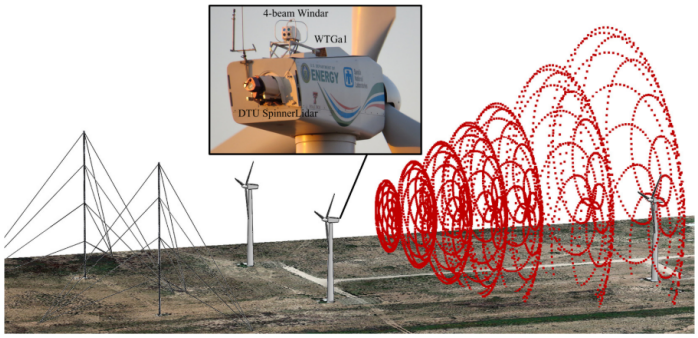

Figure 2. Schematic of SWiFT facility showing the DTU SpinnerLidar scanning patterns at several distances behind the WTGa1. An image of the installed SpinnerLidar on the rear of WTGa1 is shown. Source [7].

2.2. Data classification

As the SWiFT experiment includes wake steering study cases, we omit 10-min periods where the WTGa1 operates under high yaw misalignment. We select an average yaw error of 10° as an acceptable threshold. Figure 3-left illustrates the wind rose for the filtered and analyzed dataset at the site. Hence, we focus the analysis on the East to West winds (90°–270°) and classify data according to atmospheric stability conditions and incoming wind speeds, thus, different thrust coefficient levels (C_t). The observations are classified into atmospheric stability classes by computing the dimensionless stability parameter (z/L), where z is the height above ground, and L is the Obukhov length [8]:

$$L = -\frac{u_*^3 T}{kg\overline{w'\Theta_v'}}, \tag{1}$$

where u_* is the friction velocity, $k = 0.4$ is the von Karman constant, g is the acceleration due to gravity, T is the mean surface-layer temperature, the vertical velocity component is denoted by w, and Θ_v is the virtual potential temperature. The prime denotes fluctuations around the mean value and the overbar is a time average. We define three atmospheric stability classes based on Obukhov length range [9]: unstable ($-2 < z/L < -0.2$), near-neutral ($-0.2 < z/L < 0.2$), and stable ($0.2 < z/L < 2$) conditions. Under the assumption of stationarity and homogeneous flow, and that we are within the surface layer, Monin-Obukhov similarity theory (MOST) describes the relation between the dimensionless wind shear ϕ_m and the dimensionless stability parameter z/L. Thus, we compute ϕ_m using the polynomial form of Högström [10] and wind speed measurements of the three lowest sonic anemometers. The relation between ϕ_m and z/L from the sonic measurements at 18 m is compared to the analytical formulation in Fig. 3-middle. The measurements at this height are used to classify stability conditions at the SWiFT site. Figure 3-right shows the thrust coefficient (C_t) curve of the WTGa1 for incoming wind speeds derived from a calibrated aero-elastic model [11]. The C_t curve is obtained from simulations with uniform and steady wind with no shear.

3. Methodology

The analyzed SpinnerLidar measurements are freely available [4]. The dataset comprises line-of-sight (LOS) velocity measurements as well as the spatial location of the 984 points within each individual scan, among other information. As the SpinnerLidar measures only the radial velocity component along the beam, flow assumptions are required to reconstruct the three-dimensional wind velocity field $\mathbf{u}= (u, v, w)$, where u and v are the longitudinal and transversal

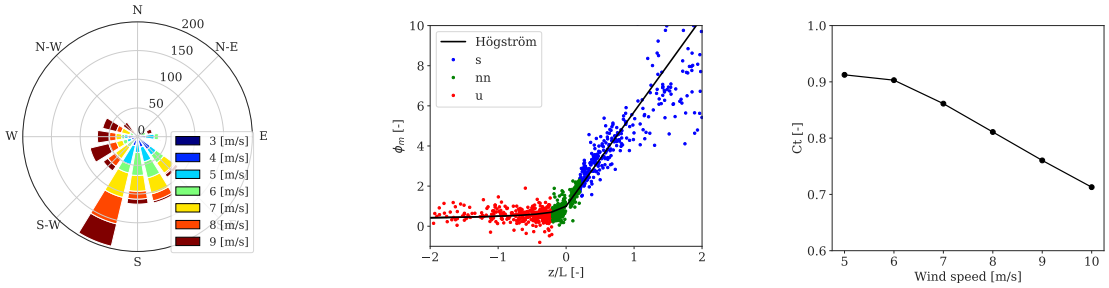

Figure 3. (Left) The wind rose of the analyzed dataset. (Middle) The dimensionless wind shear ϕ_m as function of dimensionless stability z/L. Each 10-min sample is shown in colored markers according to atmospheric stability: stable (s), near-neutral (nn) and unstable (u). (Right) The thrust coefficient curve of the WTGa1 as function of the wind speed.

velocity components. The following section describes the methodology applied to reconstruct the u-component as well as wake characteristics from the SpinnerLidar observations.

3.1. Wind speed reconstruction

The scanning geometry of the SpinnerLidar can be formulated by the elevation angle (φ_y) and the azimuth angle (φ_z). If we assume that the SpinnerLidar measures at a point, instead of over a probe volume, the LOS velocity component can be expressed in terms of the three-dimensional wind field by means of matrix rotations. This is a suitable approximation for the first statistical moment of the wind speeds measured by the SpinnerLidar at the analyzed ranges [12]. The w-component is neglected, due to the small elevation angles and the typical small values of the vertical velocity component. By including the flow direction due to yaw offset (θ), the extended form is derived as:

$$v_{LOS} = u\cos(\varphi_y)\cos(\varphi_z)\cos(\theta) - v\cos(\varphi_y)\sin(\varphi_z)\sin(\theta). \tag{2}$$

A moving average with a 15-s window is used to smoothen the yaw misalignment data in order to account for any temporal delay between the mast, nacelle and SpinnerLidar recordings due to different measurement locations. To derive the u- and v-velocity components, we formulate the points of the rosette pattern within a 2 m×2 m regular grid in the y-z plane and fit to the LOS velocity measurements for grid elements with at least two points. This procedure allows us to reconstruct the two-dimensional wind field at each snapshot of the wake. We define the normalized wake deficit as following:

$$VD(x,y,z) = \frac{U(z) - u(t,x,y,z)}{U(z)}, \tag{3}$$

where u is the instantaneous longitudinal velocity component in the wake and $U(z)$ is the 10-min mean wind speed estimated at z from multiple measurement heights at the mast by using the power law shear profile.

3.2. Wake tracking

The SpinnerLidar measurements provide the wake deficit field in a fixed frame of reference (FFoR), which is attached to the lidar coordinate system. Monitoring the wake location in time allows us to study the lateral and vertical wake movements (hereafter referred to as meandering) and to resolve wake characteristics such as velocity deficit and turbulence profiles in the meandering frame of reference (MFoR). Hence, the quasi-steady wake characteristics can

be estimated. Following the approach of [13], the wake center location (the point that would theoretically be with highest deficit if no turbulence was present) is tracked by assuming a bi-variate Gaussian function to describe the instantaneous wake shape as:

$$f_{VD} = \frac{A}{2\pi\sigma_{wy}\sigma_{wz}} \exp\left[-\frac{1}{2}\left(\frac{(y_i-\mu_y)^2}{\sigma_{wy}^2} + \frac{(z_i-\mu_z)^2}{\sigma_{wz}^2}\right)\right], \quad (4)$$

where (μ_y, μ_z) define the wake center location, $(\sigma_{wy}, \sigma_{wz})$ are width parameters of the wake profile in the y and z directions, respectively, (y_i, z_i) denote the spatial location of the LOS and A is a scaling parameter. Therefore, the measured wake deficits from Eq. 3 are fitted to Eq. 4 through a least-squares fitting procedure. To ensure the quality of the fitting, we reject scans where the estimated wake center location is within $\approx 10\%$ of the lateral bounds of the scanning area and at more than 0.75 D distance from the hub height in the vertical direction.

4. Results

The mean inflow wind characteristics of the analyzed dataset are presented in Table 1. The data includes wind speeds in the range 3–9 m/s, i.e., covering a wide range of wind turbine operation conditions below rated wind speed, and a number of different stability conditions. The influence of atmospheric stability is clearly visible on the inflow wind statistics. Stable conditions are associated with strong wind shears and low turbulence levels. The former decreases, and the latter increases, as the atmosphere becomes more unstable. We concentrate the analysis of the SpinnerLidar data at multiple ranges (2, 3, 4 and 5 D), when assessing the velocity deficit profile. We exclude near-wake measurements ($<$ 2 D), as we are primarily interested in the far-wake characterization, which dominates power and load levels within wind farms. The SpinnerLidar measurements at 2.5 D distance are used to derive turbulence and meandering statistics of the wake.

Table 1. Average inflow wind characteristics from sonic observations at 32 m classified into wind speed ranges with interval of ±0.5 m/s and atmospheric stability classes: stable (s), near-neutral (nn) and unstable (u). The number of samples refer to 10-min periods, α denotes the wind shear and $TI = \sigma_U/U$ is the turbulence intensity. The variances of the v- and w-velocity components are also provided (σ_v^2,σ_w^2). The rows highlighted in grey refer to periods where the SpinnerLidar measures at a fixed distance of 2.5 D.

U $[m/s]$	Samples [-]			α [-]			TI [%]			σ_v^2 $[m^2/s^2]$			σ_w^2 $[m^2/s^2]$		
	s	nn	u	s	nn	u	s	nn	u	s	nn	u	s	nn	u
3	8	4	15	0.42	0.46	0.07	8	18	26	0.03	0.40	0.96	0.01	0.13	0.32
4	19	5	16	0.36	0.09	0.08	8	20	22	0.09	0.77	1.11	0.09	0.16	0.38
5	28	6	17	0.28	0.12	0.01	7	10	22	0.15	0.61	1.32	0.03	0.13	0.39
	5	2	6	0.37	0.12	0.01	7	14	13	0.11	0.63	0.46	0.01	0.11	0.18
6	32	9	24	0.28	0.17	0.04	7	12	16	0.15	1.21	1.32	0.06	0.15	0.37
	1	2	7	0.39	0.25	0.01	6	10	12	0.05	0.48	1.00	0.01	0.13	0.34
7	15	16	18	0.23	0.12	0.03	7	12	14	0.26	0.74	1.65	0.08	0.25	0.42
	11	2	9	0.25	0.25	0.05	9	10	12	0.37	0.48	0.83	0.17	0.29	0.38
8	8	13	6	0.26	0.08	0.04	7	13	12	0.55	1.06	0.93	0.10	0.32	0.38
9	5	12	3	0.30	0.17	0.02	7	11	9	0.32	0.70	1.17	0.13	0.33	0.30

4.1. Velocity deficit

The mean velocity deficit profile for an incoming wind speed of 6 m/s under stable conditions is shown in Fig. 4. The wake exhibits a well-defined radial symmetry at the analyzed downstream distances. We observe a strong velocity deficit, which persists moving downstream and a slight wake expansion. The low wake-expansion and wake recovery rates are related to low ambient turbulence intensity, which limits the turbulence mixing in the wake regions, as expected [5].

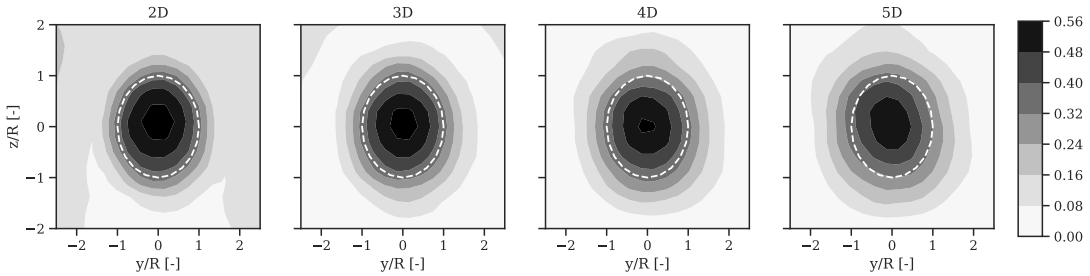

Figure 4. Ensemble-averaged wake deficit profile in the MFoR for inflow wind speed of 6 m/s under stable conditions. The rotor area is illustrated by dashed white lines. The vertical and lateral directions are normalized over the rotor radius and centered at hub height.

We illustrate the mean wake deficit profiles for different inflow wind speeds and stability conditions in Fig. 5. The span-wise velocity deficits at hub height are shown in the MFoR. The wake deficit exhibits a Gaussian-like shape, as already observed in previous studies [5]. The influence of atmospheric stability on the wake deficit can be seen in Fig. 5-top. The wake recovers faster as the atmosphere becomes more unstable. These effects are caused by the enhanced turbulent mixing in the wake due to higher ambient turbulence, which increases the recovery of the velocity deficit. In order to investigate the effects of rotor thrust coefficients on the wake deficit, we select periods characterized by stable atmospheric conditions and analyze three wind speed ranges, 5, 6 and 9 m/s, with turbulence intensity levels below 8%. The wake deficit profiles are shown in Fig. 5-bottom. There, we find a faster recovery of the wake deficit at 9 m/s ($C_t \approx 0.75$, see Fig. 3-right) compared to the lower wind speeds ($C_t \approx 0.85$–0.90). Although C_t levels exhibit a secondary effect compared to the incoming turbulence, smaller wake deficits are expected for wind turbine operation above rated wind, where C_t significantly drops due to blade pitching. These results indicate that both rotor thrust coefficient and ambient turbulence effects should be included in analytical wake models. The former affects the wake-generated turbulence, enhanced by the high C_t and strong velocity deficit; the latter affects the degree of turbulence mixing in the wake. As observed, both contribute to the wake recovery rate.

4.2. Turbulence

The analysis focuses on the dataset, where the SpinnerLidar is measuring at a single focus distance of 2.5 D. We describe the wake turbulence intensity in terms of $TI = \sigma_U/U$, where U is the mean longitudinal velocity component. The probe volume filtering effects on the LOS variance at 2.5 D are neglected. We investigate the influence of atmospheric stability on the spatial distribution of wake turbulence, by selecting 10-min periods with similar incoming wind

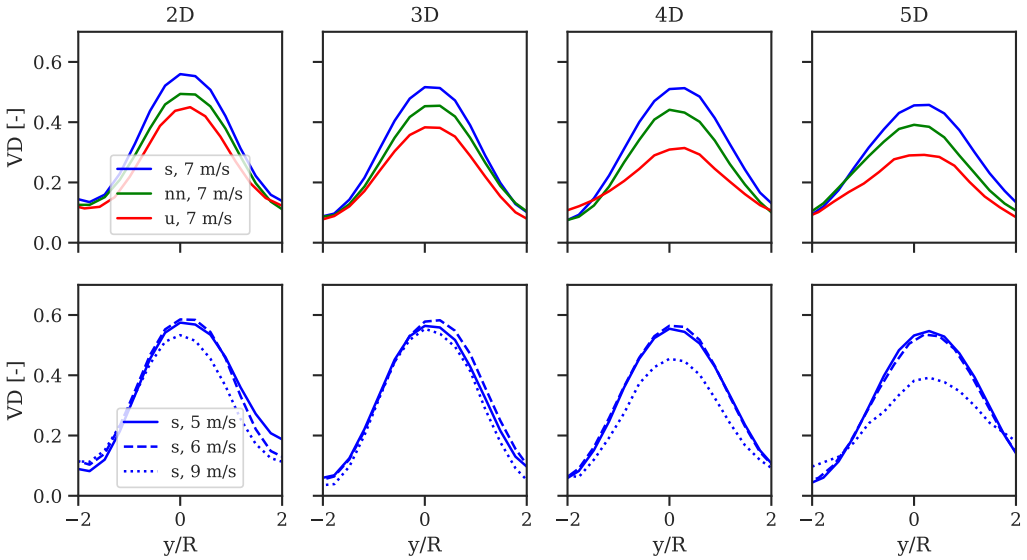

Figure 5. Comparison of the lateral velocity deficit at hub height in the MFoR as function of stability: stable (s), near-neutral (nn) and unstable (u) (top row) and as function of inflow wind speeds for stable regimes (bottom row).

speed. Thus, we select periods with inflow wind speed of 5 m/s and TI = 8, 9 and 10 % for the stable, near-neutral and unstable case, respectively. The span-wise turbulence distribution in the FFoR and MFoR is shown in Fig. 6-left. The turbulence resolved in the FFoR can be described, according to the DWM formulation, by the contribution of ambient turbulence, wake-added turbulence and the 'apparent' turbulence due to meandering of the velocity deficit [2]. As a result, the lower TI under stable condition (blue dotted-line), compared to near-neutral and unstable regimes, can be explained by the inherent low amplitude of meandering. This is demonstrated in Fig. 6-right, where the time series of the wake center displacement is shown. We observe a significantly lower wake movement under stable compared to near-neutral and unstable conditions. Besides, a lateral deflection of wake center position with respect to the rotor center ($y/R = 0$) is seen, which is due to a slight yaw misalignment. The turbulence resolved in the MFoR is lower compared to that in the FFoR (see Fig. 6-left), as expected, due to the high-pass filtering intrinsic of the transformation, which filters out the large meandering scales. In the MFoR, we can observe a more symmetric turbulence profile with respect to the rotor center. Besides, two distinctive peaks are found at $y/R \approx \pm 1$, in correspondence with the location of maximum velocity gradients.

We analyze the lateral turbulence distribution at hub height in the MFoR under different atmospheric stability conditions and incoming wind speeds from Table 1. Turbulence resolved in the MFoR is composed of ambient and wake-generated turbulence; the latter is caused by the large wake velocity gradients and blade bound vortex developing mainly at the blade root and tip trailing edges [2]. Figure 7-left shows the mean turbulence profile at 5 m/s and 7 m/s under stable regimes. The two peaks can be clearly seen in proximity of the rotor tip regions ($y/R \approx \pm 1$), whereas an inner peak is also observed. The outer peaks define the layer between the wake and the ambient flow, whereas the inner peaks delimit the region between the wake behind the nacelle and the outer wake [15]. Figure 7-middle illustrates the mean turbulence profiles for incoming wind speed of 6 m/s and 7 m/s under near-neutral conditions. Although

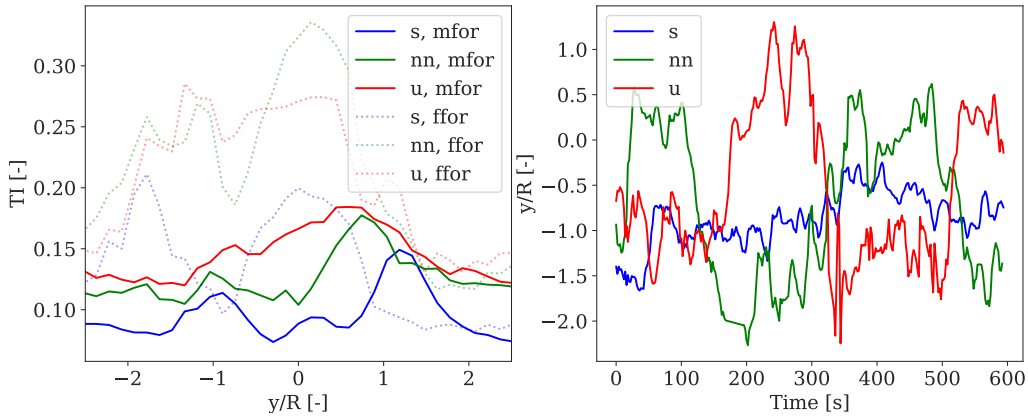

Figure 6. (Left) Comparison of span-wise profiles of wake turbulence in the MFoR (solid lines) and FFoR (dotted lines) for different atmospheric stability conditions: stable (s), near-neutral (nn) and unstable (u). The lateral coordinate is normalized over the rotor radius and centered at hub height. (Right) Comparison of wake center displacement in the lateral direction as function of time.

two peaks are seen at 6 m/s, these peaks gradually vanish for increasing turbulence intensity levels. This behaviour is also consistent with the observation under unstable conditions in Fig. 7-right, where the turbulence distribution becomes more uniform as a result of the enhanced mixing.

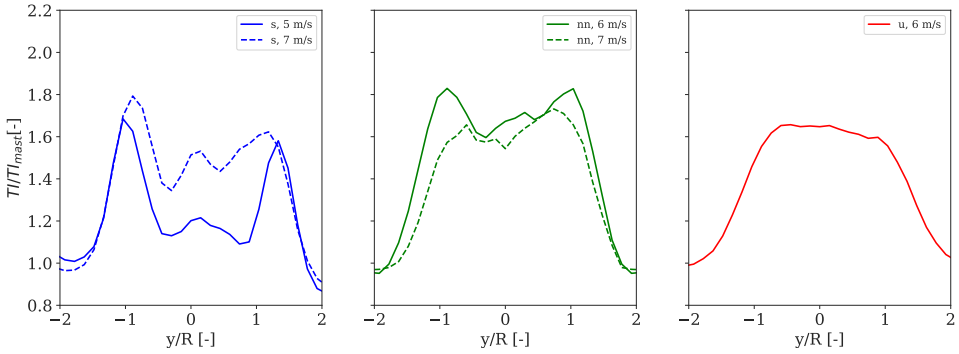

Figure 7. Comparisons of the lateral profiles of the wake turbulence normalized over the ambient turbulence at hub height. The stability classes are identified by different colours and inflow wind speeds by different line styles as described in the legend. The lateral coordinate is normalized over the rotor radius and centered at hub height.

Figure 8 shows the vertical turbulence profiles resolved in the MFoR at 7 m/s for different atmospheric stability conditions. The profiles show an asymmetric behavior, where enhanced turbulence levels are observed in the upper wake edge in proximity of the rotor top tip region ($z/R \approx 1$). This effect originates from the strong velocity gradient (see dotted-lines in Fig.8) and turbulence from blade tip vortices. A more uniform turbulence distribution is seen under unstable conditions.

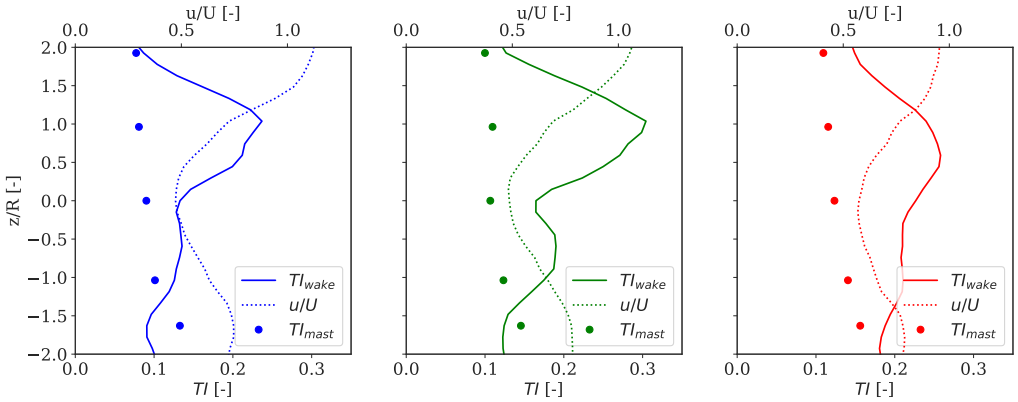

Figure 8. Comparisons of vertical profiles of the ambient turbulence (circles), wake turbulence in MFoR (solid lines) and the u-velocity component in wake normalized over the wind speed at hub height U (dotted-lines). The colours indicate atmospheric stability: stable (blue), near-neutral (green) and unstable (red). The vertical coordinate is normalized over the rotor radius and centered at hub height.

4.3. Wake meandering

The amplitude of wake meandering is quantified as the standard deviation of the wake center displacements in the lateral and vertical directions normalized over the rotor diameter, (σ_{μ_Y}/D and σ_{μ_Z}/D), respectively. Table 2 provides the ensemble-averaged statistics of wake meandering measured at 2.5 D relative to different atmospheric conditions. We observe that wake movements are larger in the horizontal plane than in the vertical plane by a factor of ≈2–3.5. Besides, the magnitude of meandering increases under unstable compared to stable conditions, as expected.

Table 2. Average statistics of the normalized wake meandering amplitudes in the lateral and vertical directions (σ_{μ_Y}/D and σ_{μ_Z}/D) under three atmospheric stability conditions. The mean inflow wind characteristics recorded at the 32-m sonic are also provided. The number of samples refer to 10-min periods.

Stability	Samples [-]	σ_u [m/s]	σ_v [m/s]	σ_w [m/s]	σ_v/σ_w [-]	σ_{μ_Y}/D [-]	σ_{μ_Z}/D [-]
Stable	15	0.67	0.55	0.36	1.50	0.21	0.06
Near-neutral	17	0.92	0.75	0.49	1.53	0.30	0.11
Unstable	18	0.84	0.80	0.51	1.55	0.30	0.14

The wake meandering can be modeled by considering the wakes to act as passive tracers driven by the large-scale turbulence structures in lateral and vertical directions [2]. To 'isolate' large-scale turbulence structures, we apply a low-pass filter to the v- and w-velocity time series measured at the mast by assuming a 'cut-off eddy size' of two rotor diameters as proposed in [2]. The meandering behavior as function of low-pass filtered statistics is shown in Fig. 9. A correlation between the wake displacements and $\sigma_{v_{LP}}$ and $\sigma_{w_{LP}}$ levels is observed. Besides, observations under stable conditions are characterized by lower meandering compared to those under near-neutral and unstable conditions. However, further investigation is needed

to determine more precisely which turbulence structures contributes to the meandering process.

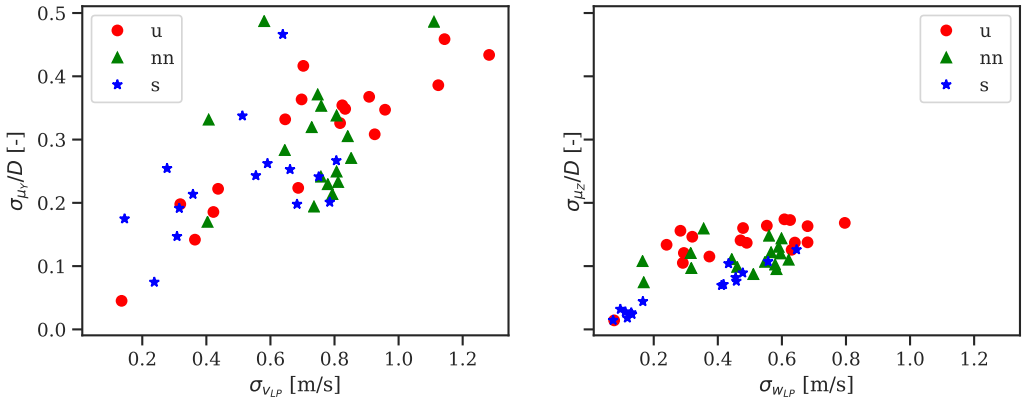

Figure 9. Normalized wake meandering amplitudes in the lateral (left) and vertical (right) direction as a function of the standard deviation of the low-pass filtered v and w-velocity component measured at the mast. Each marker refers to a 10-min period.

5. Discussion

SpinnerLidar measurements of the wake flow field behind an operating wind turbine are analyzed. We derive wind and turbulence intensity fields in the wake region and estimate wake meandering statistics relative to several inflow wind conditions. In order to derive the quasi-steady wake characteristics in the MFoR, we apply a wake-tracking technique based on a bi-variate Gaussian wake shape function. Although this procedure is proven to be robust under stable conditions (low turbulence levels), an increasing number of scans are 'rejected' as the atmosphere becomes more unstable and the scanning area increases. These scans are either characterized by multiple low wind speed areas or by wake center location in proximity of the edges of the scanning area. These effects occur as the size of turbulent structures becomes comparable to that of the wake deficit. The lidar-estimated turbulence is subjected to volume averaging and cross-contamination effects [14]. The filtering effect due to the probe volume tends to reduce the radial velocity variance when compared to a point measurement. The ratio of the filtered to the unfiltered radial velocity variance accounts for approximately 12 % for the DTU SpinnerLidar scanning at 2.5 D under near-neutral conditions [6]. As the Doppler radial velocity spectrum is available for the SWiFT campaign, in a future study we will estimate the unfiltered radial velocity variance and provide more accurate estimates of wake-added turbulence. Furthermore, the proposed methodology and the derived wake characteristics will be applied to calibrate the DWM model for load validation purposes.

6. Conclusions

The SpinnerLidar measurements of the wake flow field collected from an experiment at the SWiFT facility were analyzed to investigate wake behaviour under different atmospheric conditions. The analysis focused on the spatial distribution and magnitude of the wake deficit, wake-added turbulence and meandering, which are key aspects for power and load prediction assessments. The wake deficit can be approximated by a Gaussian-like shape, which recovers

faster under unstable compared to neutral and stable conditions, due to enhanced turbulent mixing. The wake turbulence profile under stable conditions exhibited two distinct peaks in proximity of the rotor tips, while a more uniform turbulence distribution was observed for unstable conditions. The wake meandering amplitude was found to be driven by large-scale turbulence structures as well as turbulence levels. Overall, the analyzed SpinnerLidar measurements of the wake flow field are suitable for calibration and validation of wake models.

Acknowledgments

Sandia National Laboratories is a multi-mission laboratory managed and operated by National Technology and Engineering Solutions of Sandia, LLC., a wholly owned subsidiary of Honeywell International, Inc., for the U.S. Department of Energy's National Nuclear Security Administration under contract DE-NA-0003525.

References

[1] Larsen T J, Madsen H A, Larsen G C and Hansen K S 2013 *Wind Energy.* **16** 605-624
[2] Madsen H A, Larsen G C, Larsen T J, Troldborg N and Mikkelsen F R 2010 *J. Solar En. Eng.* **132** 041014
[3] Reinwardt I, Gerke N, Dalhoff P, Steudel D and Moser W 2018 Validation of wind turbine wake models with focus on the dynamic wake meandering model *J. Appl. Phys.* **1037** 072028
[4] Herges T G, Maniaci D C, Naughton B T, Mikkelsen T and Sjöholm M. 2017 High resolution wind turbine wake measurements with a scanning lidar *J. Phys.: Conf. Ser.* **854** 012021
[5] Doubrawa P, Debnath M, Moriarty P J, Branlard E, Herges T G, Maniaci D C and Naughton B 2019 Benchmarks for Model Validation based on LiDAR Wake Measurements *J. Phys.: Conf. Ser.* **1256** 012024
[6] Peña A, Mann J and Gunhild R T 2019 SpinnerLidar measurements for the CCA V52 *DTU Wind Energy* E-Report-0177
[7] Herges T G and Keyantuo P 2019 Robust Lidar Data Processing and Quality Control Methods Developed for the SWiFT Wake Steering Experiment *J. Phys.: Conf. Ser.* **1256** 012005
[8] Obukhov A M 1971 *Boundary-layer Meteorology* **2** 7–29
[9] Peña 2019 *J. of Renewable and Sustainable Energy* **11** 063302
[10] Högström U 1988 *Boundary-layer Meteorology* **42** 55-78
[11] Kelley C L and White J 2018 An Update to the SWiFT V27 Reference Model *Sandia National Laboratories* SAND2018-11893
[12] Debnath M, Doubrawa P, Herges T G, Martinez-Tossas L A, Maniaci D C, Moriarty P J 2019 Evaluation of Wind Speed Retrieval from Continuous-Wave Lidar Measurements of a Wind Turbine Wake Using Virtual Lidar Techniques *J. Phys.: Conf. Ser.* **1256** 012008
[13] Trujillo J J, Bingöl F, Larsen G C, Mann J and Kühn M 2011 *Wind Energy* **14** 61-75
[14] Peña A, Mann J and Dimitrov N 2017 *Wind Energy Science* **2** 133-152
[15] Foti D, Yang X and Sotiropoulos F 2018 *J. of Fluid Mechanics* **842** 5-25